Direct numerical simulations of anisotropic diffusion of spherical particles in sedimentation

Adnan Hamid* and Ryoichi Yamamoto†
Department of Chemical Engineering, Kyoto University, Kyoto 615-8510, Japan
(Received 12 December 2012; published 27 February 2013)

We investigated the scaling of the hydrodynamic velocity fluctuations and self-diffusion in the sedimentation of monodispersed spherical particles via direct numerical simulations using the smoothed profile method over a moderate range of volume fractions ($0.01 \leqslant \phi \leqslant 0.12$). Hydrodynamic velocity fluctuations are visible at large Peclet numbers (Pe), and they scale as $(\phi L/a)^{1/2}$ at low volume fractions ($\phi \leqslant 0.04$). Their characteristics become independent of volume fraction at moderate volume fractions ($0.06 \leqslant \phi \leqslant 0.12$). Both vertical and horizontal self-diffusion coefficients scale as $(L/a)^{3/2}\phi^{1/2}$ at low volume fractions. At moderate volume fractions, the vertical diffusion scales as $(L/a)^{3/2}\phi^{-1/2}$; in contrast, the horizontal diffusion is saturated with respect to volume fraction. The diffusion anisotropy increases with increasing Pe and saturates at high Pe values. The saturated value remains unchanged at low volume fractions, whereas further increase in the volume fraction decreases this anisotropy. The reduction of this anisotropy is attributed to the $\phi^{-1/2}$ scaling of the vertical relaxation time at moderate volume fractions; however, the horizontal relaxation time is independent of the volume fraction at this regime.

DOI: 10.1103/PhysRevE.87.022310 PACS number(s): 82.70.Dd, 31.15.xv, 46.15.−x, 82.20.Wt

I. INTRODUCTION

The settling of particles in a viscous fluid is a fundamental phenomenon of nonequilibrium suspension dynamics, but the topic is extremely challenging to examine because accurately characterizing the long-range many-body interactions between the particles proves difficult. These interparticle interactions, caused by fluid flow, are referred to as hydrodynamic interactions (HIs). These HIs may decay as slowly as $1/r$, strongly affecting the dynamic behavior of the suspension. Although many experimental [1–6], theoretical [7–9], and numerical [10–25] investigations have been performed to provide a basic understanding of sedimentation, knowledge of the HIs remains incomplete. Significant progress was made by Batchelor [26], who explained the hindered settling of the sedimenting particles and obtained an expression of the form $V_s = V_s^{\phi=0}(1 - k\phi)$ in which $V_s^{\phi=0} = \frac{2}{9}ga^2(\rho_p - \rho_f)/\eta$ represents the Stokes velocity [27] of a single particle, a is the particle radius, ρ_p is the particle density, ρ_f is the fluid density, g is the gravitational acceleration, η is the fluid viscosity, ϕ is the particle volume fraction, and k is a constant that shows the effect of fluid backflow [28].

Due to the constantly changing configuration of the suspension microstructure, the velocity of the individual particles fluctuates around their mean settling velocity. Inconsistencies exist between the experiments [1,2], and the simulations [13] and theory [7,8]; the velocity fluctuations predicted by the theory and numerical simulations depend on the system size, but the experiments exhibit no such dependency. Subsequent studies have shown that if the simulations exhibit dependence on container size, some screening or cutoff length scale must exist in the suspension microstructure that depends on the particle volume fraction [29]. This inconsistency was solved by Segre *et al.* [4], who introduced the concept of a characteristic swirl size or correlation length: Velocity fluctuations are explained as a function of cell size only when the cell size is less than the swirl size. These results were later confirmed by Nguyen and Ladd [14], using the lattice Boltzmann method (LBM). These velocity fluctuations are strongly anisotropic, with the vertical velocity fluctuations larger than the horizontal.

The disagreement between the experiments and the early simulations stimulated further work to address the nature of the screening mechanism for the velocity fluctuations (i.e., the manner in which correlations in the fluctuations decay over time and space). Shaqfeh and Koch [8] proposed a Debye-like screening, and Ramaswamy [30] proposed a stochastic convection-diffusion model; however, these ideas were not confirmed by the simulations of Ladd *et al.* [10–14]. Hinch [31] suggested another mechanism in which the bottom wall acts as a sink for fluctuations. This mechanism was confirmed using simulations [13,14]. Some authors [6,14] posited that stratification and polydispersity also play key roles in screening. More details can be found in Guazzelli's review paper [32].

Self-diffusion is one of the most important parameters of sedimentation due to its role in mixing and other chemical processes. This diffusion is referred to as hydrodynamic diffusion because it originates in the HIs between the particles. As with the velocity fluctuations, hydrodynamic diffusion obtained from the simulations is affected not only by the size of the simulation box but also by its shape. Diffusion is also strongly anisotropic, with vertical diffusion greater than horizontal. This anisotropic behavior arises from the anisotropic nature of the velocity fluctuations and their relaxation times [33]. Early self-diffusion simulations [10] yielded a large value for this anisotropy. A more realistic value of the anisotropy was later obtained by Ladd [12] and Cunha [19]; the former increased the aspect ratio of the periodic box, and the latter used dynamic simulations with an impenetrable lower boundary. Despite the importance of hydrodynamic diffusion in industrial chemical research, few simulations [10,11,18,19] have been performed to address its behavior.

Under sedimentation, the microstructure of the suspension is determined by the long-range HIs, which are characterized by large time and length scales, features that render the

*hamid@cheme.kyoto-u.ac.jp
†ryoichi@cheme.kyoto-u.ac.jp

nonequilibrium properties of the colloidal particles challenging to simulate. Different methods [10,18,19,34–36] are available to simulate the nonequilibrium colloidal phenomena, e.g., Stokesian dynamics [34], LBM [10–15], dissipative particle dynamics [35], stochastic rotation dynamics (SRD) [16], and direct numerical simulations (DNS) [19]. More details on these methods are presented by Padding *et al.* [17] and Ladd *et al.* [15]. In this study, we used DNS with the smoothed profile (SP) method, which replaces the original sharp boundaries between the particle and the host fluid with a diffuse interface of finite thickness. This approach enabled us to use a fixed Cartesian grid, thereby significantly improving the speed of the numerical computations. A similar smoothed profile [37] was adopted in the previously proposed fluid-particle dynamics (FPD) method in which particles are modelled by a highly viscous fluid. We treated the particles as nondeformable solids such that no additional constraints arose.

Unlike most previous studies [3,5,13,19], which were performed in a non-Brownian regime (Pe $\rightarrow \infty$), we focused our work in the finite Peclet number (Pe) regime with different volume fractions and system sizes. Sedimentation at finite Pe values describes the relative effects of thermal fluctuations (caused by collisions between colloids and solvent particles) and hydrodynamic fluctuations (caused by hydrodynamic flows of the solvent). We investigated the imprints of these relative effects on the anisotropic behavior of the velocity fluctuations and diffusion. Padding *et al.* [16–18] were the first to simulate sedimentation at a finite Pe using coarse-grained SRD simulations. The simplified dynamics allowed accurate calculation of the transport properties; however, due to its stochastic nature, SRD is less effective than pre-averaged LBM for large Pe. In SRD, the highest achievable Pe is limited by the constraints on the Mach and Reynolds numbers (Re), whereas in the SP method, the highest Pe is limited only by Re. Consequently, a wide range of Pe is achievable using our method. Padding [16–18] focused his work in the low volume fraction regime. The present work not only validates the work of Padding at low volume fraction but also explores the effects of moderate volume fraction on velocity fluctuations and anisotropic diffusion.

The main objective of the present study is to investigate the relative effects of thermal and hydrodynamic forces on velocity fluctuations and particle diffusion for different volume fractions. In the previous studies [38,39], we have examined the finite Pe effects at a single volume fraction ($\phi = 0.02$), whereas in the present study, we investigated the scaling relations of hydrodynamic velocity fluctuations and self-diffusion at different system sizes and volume fractions. Working along the lines of Caflish and Luke [7], Hinch [31] previously suggested the scaling of velocity fluctuations and self-diffusion, which is valid for a low volume fraction. However, the high volume fraction regime requires additional attention. This paper provides insights into the anisotropic behavior of diffusion at finite Pe. We also suggest valid scaling relations of the velocity fluctuations, their relaxation times, and self-diffusion for a moderate volume fraction regime. In this paper, Sec. II explains the simulation method, and Sec. III describes the selection of the working parameters. The results are provided in Sec. IV, and we present conclusions based on our work in Sec. V.

II. SIMULATION METHOD

In the SP method, the colloid surface is not treated as a sharp interface lacking thickness, but an intermediate region is introduced at the surface. This intermediate region or interface has a width comparable to or larger than the grid spacing, and the colloid's density profile is defined such that it changes smoothly within that interface. Quantities such as the velocity and pressure are defined over the entire computational domain, which includes the colloid and the solvent. A smoothed profile function [36] $0 \leqslant \phi(\boldsymbol{x},t) \leqslant 1$ is used to distinguish between the fluid and particle domains in which $\boldsymbol{x}$ denotes the particle spacial position. Here, $\phi = 0$ stands for fluid, $0 < \phi < 1$ describes the interface and $\phi = 1$ represents the particle domain. In this section, we briefly explain the salient features of our method. The detailed formulas, algorithm, and applicability of the SP method can be found in the literature [36,40–44].

The motion of the ith colloidal particle is obtained by solving Newton's equations of motion:

$$M_i \dot{\boldsymbol{V}}_i = \boldsymbol{F}_i^{\mathrm{H}} + \boldsymbol{F}_i^{\mathrm{c}} + \boldsymbol{F}_i^{\mathrm{ext}} + \boldsymbol{G}_i^{\mathrm{V}}, \quad \dot{\boldsymbol{R}}_i = \boldsymbol{V}_i \tag{1}$$

$$\boldsymbol{I}_i \cdot \dot{\boldsymbol{\Omega}}_i = \boldsymbol{N}_i^{\mathrm{H}} + \boldsymbol{N}_i^{\mathrm{ext}} + \boldsymbol{G}_i^{\Omega}, \tag{2}$$

in which $\boldsymbol{R}_i$ is the position of the particle, and $\boldsymbol{V}_i$ and $\boldsymbol{\Omega}_i$ are the translational and rotational velocity of the particle, respectively. The mass and moment of inertia are denoted by M_i and $\boldsymbol{I}_i$, respectively. The hydrodynamic torque and force exerted by the solvent on the particle are represented by $\boldsymbol{N}_i^{\mathrm{H}}$ and $\boldsymbol{F}_i^{\mathrm{H}}$, respectively. The $\boldsymbol{F}_i^{\mathrm{ext}}$ and $\boldsymbol{N}_i^{\mathrm{ext}}$ are the external force and torque, respectively. The $\boldsymbol{G}_i^{\mathrm{V}}$ and $\boldsymbol{G}_i^{\Omega}$ are the random force and torque due to thermal fluctuations, which can be described as $\langle \boldsymbol{G}_i^n(t)\boldsymbol{G}_j^n(0)\rangle = \alpha^n \boldsymbol{I}\delta(t)\delta_{ij}$ in which $\langle \boldsymbol{G}_i^n(t)\rangle = 0$ and α^n $(n \in \mathrm{V},\Omega)$ is the parameter that controls the temperature of the system T. The actual value of the particle temperature is determined using the long-time diffusion coefficient of the equilibrium system. When simulating a Brownian particle using HIs, the diffusion coefficient is affected by the finite size effects (i.e., artifacts arise when the system size is smaller than the correlation length). These effects can be accounted for by ${D_0}^{\phi=0} = D_0 K(\phi)$, in which ${D_0}^{\phi=0}$ is the thermal diffusion coefficient of a Brownian particle at infinite dilution, D_0 is the thermal diffusion coefficient of Brownian particles obtained for $\phi \neq 0$, and $K(\phi)$ is the coefficient that represents the effects of the finite volume fraction of dispersed particles under periodic boundary conditions [45]. Finally, the temperature of the system can be determined using the Stokes-Einstein equation, $k_{\mathrm{B}}T = 6\pi\eta a {D_0}^{\phi=0}$. The detailed implementation of Brownian motion in some test cases is presented by Iwashita *et al.* [41]. Direct interparticle interactions are denoted by $\boldsymbol{F}_i^{\mathrm{c}}$, and we represent these interactions as a truncated Lennard-Jones (LJ) potential with the large powers of 24:12, which can be defined as follows:

$$U_{\mathrm{LJ}}(r_{ij}) = \begin{cases} 4\epsilon\left[\left(\frac{\sigma}{r_{ij}}\right)^{24} - \left(\frac{\sigma}{r_{ij}}\right)^{12}\right] + \epsilon & \left(r_{ij} \leqslant 2^{\frac{1}{12}}\sigma\right), \\ 0 & \left(r_{ij} > 2^{\frac{1}{12}}\sigma\right), \end{cases} \tag{3}$$

in which $r_{ij} = |\boldsymbol{R}_i - \boldsymbol{R}_j|$. The parameters σ and ϵ denote the length and energy units of the LJ potential, respectively, with $\sigma = 2a$ representing the particle diameter.

In the SP method, the solvent motion is obtained by solving the modified Navier-Stokes equation:

$$\rho_f(\partial_t \boldsymbol{v} + \boldsymbol{v}\cdot\nabla\boldsymbol{v}) = -\nabla p + \eta\nabla^2\boldsymbol{v} + \rho_f\phi\boldsymbol{f}_p \qquad (4)$$

for the total velocity field $\boldsymbol{v}$ and the pressure field p under the incompressibility condition ($\nabla\cdot\boldsymbol{v}=0$). The rigidity of the particle and the fluid/particle nonslip boundary conditions are incorporated through the body force $\phi\boldsymbol{f}_p$ [36,40]. Moreover, an estimation of the error [46], a comparison of the SP method with the force-coupling method (FCM) [47], and a high resolution DNS [48] based on high-order spectral/*hp* element discretization on hybrid grids revealed that, compared with FCM and aforementioned DNS scheme, the SP method is computationally less expensive and advantageous for simulating moving particles because it avoids complex discretizations around the particles. This study simulated many test cases and found that the SP method accurately resolves the near-field and far-field flows.

III. SIMULATION PARAMETERS

A number of simulations were performed under periodic boundary conditions with a volume fraction ranging from 0.01 to 0.12. In the present study, we divide the range of volume fractions into a low volume fraction regime defined as $\phi \leqslant 0.04$ and a moderate volume fraction regime defined as $0.06 \leqslant \phi \leqslant 0.12$. This division helps to explain the scaling of the hydrodynamic velocity fluctuations and the self-diffusion in an effective way, which will be explained later. Three different cubic periodic boxes of dimensions $L = 64\Delta$, 128Δ, and 256Δ were used and the particle size was held constant at 4Δ for all simulations in which the grid spacing Δ is taken as the unit of length. For given values of η and ρ_f, the remaining units of mass, time, pressure, and energy are defined as $\rho_f\Delta^3$, $\rho_f\Delta^2/\eta$, $\eta^2/\rho_f\Delta^2$, and $\eta^2\Delta/\rho_f$, respectively. The thermal fluctuations k_BT were maintained at $\sim$0.3, and the ϵ of the LJ potential was set at 2.5. Gravity was introduced in the z direction, and the Pe was increased by increasing the gravitational force. We held the particle-to-fluid-density ratio at 5 to have a large range of Pe. The center-of-mass of the whole fluid is constant to avoid an indefinite acceleration of the system.

In this study, the range of Pe is achieved by increasing the value of gravity, which is introduced in the z direction. The increase in gravity also increases the Reynolds number, $\mathrm{Re} = \rho_f a V_s^{\phi=0}/\eta$ from 10^{-3} to 0.2, which is low enough to ignore the inertial effects and remains within the Stokes regime. In contrast to the simulations studies [18,19], most of the experiments [1,2,4,32] have been performed at low Re values, usually of the order of 10^{-5} or less. Because a relative deviation from the Stokes regime scales with the square of Re, we can probe relatively high Re values without straying from the relevant experimental conditions. In addition, maintaining such a low value of Re is computationally more expensive. For a given initial configuration, particles require a certain time to acquire their steady-state velocities and positions. We monitored the data, and only that corresponding to the steady-state velocities is used. The simulations are run up to $500t_s$ for $\mathrm{Pe}=0.7$ and to $1200t_s$ for $\mathrm{Pe}>50$; sufficient to yield statistically meaningful data for the analysis in which t_s denotes the Stokes time.

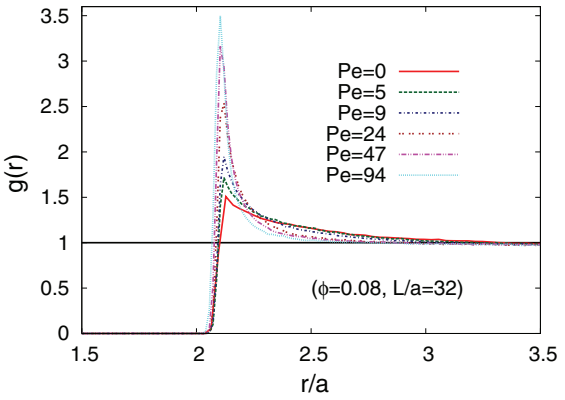

FIG. 1. (Color online) Radial distribution function $g(r)$ for different Pe values. Simulations are performed in a cubic periodic box of length $L/a = 32$ with a particle size of $a = 4$, keeping ϕ and k_BT constant at $\approx$0.08 and 0.3, respectively.

The Peclet number, which is the ratio of convection to diffusion, can be defined as follows:

$$\mathrm{Pe} = \frac{a V_s^{\phi=0}}{D_0}. \qquad (5)$$

One can expect HIs to play a dominant role at higher Pe values, thereby leading to changes in the microstructure. The HIs are increased with an increase in Pe. The additional hindrance caused by these HIs changes the microstructure of the system. A quantitative measure of the microstructure at the particle scale is provided by the radial distribution function (RDF),

$$g(r) = \frac{2L^3}{N^2}\left\langle \sum_{i<j}\delta(\boldsymbol{r}-\boldsymbol{r}_{ij})\right\rangle, \qquad (6)$$

in which N is the total number of particles, $r = |\boldsymbol{r}|$, $\boldsymbol{r}_{ij} = \boldsymbol{R}_i - \boldsymbol{R}_j$, $\langle\cdots\rangle$ denotes an ensemble average, and the summation $\sum_{i<j}$ is taken over all particle pairs. The definition of $g(r)$ is such that $4\pi\rho g(r)r^2\Delta r$ represents the mean number of particles in a shell of radius r and thickness Δr that surrounds a particle at the origin [49]. Figure 1 shows the $g(r)$ for different Pe values for a system of size $L/a = 32$ and $\phi = 0.08$. The peak of the function increases with increasing Pe, demonstrating the formation of aggregates or particle clusters in close contact. This clustering is induced by the dominance of hydrodynamic forces with increasing Pe, which, in turn, progressively reduces the effects of random motion. A similar phenomena has also been observed by Brady *et al.* [50] in their investigation of the relative effects of thermal and shear forces. They reduced the effects of thermal fluctuations by increasing the shear rate and observed a similar cluster formation. Apart from the initial peak, the results are indistinguishable from the equilibrium results for $\mathrm{Pe} \leqslant 9$, demonstrating the strong effect of the thermal fluctuations. For $\mathrm{Pe} > 9$, these results are differentiable, providing evidence that the HIs exert a progressively dominating effect. A relatively large change in the RDF at $\mathrm{Pe} \geqslant 24$ indicates that the HIs overpower the sedimentation phenomena. Moreover, the peak of $g(r)$ at $\mathrm{Pe} = 0$ is higher than the peak value provided by the well-known exact solution [51,52] of the Percus-Yevick (PY) integral equation for the RDF. In our results, this discrepancy arises from an overlapping

of the smoothed profiles of two particles in close contact. Similar discrepancies are also reported in the literature [18].

IV. RESULTS AND DISCUSSION

A. Hydrodynamic velocity fluctuations and their scaling

One of the main objectives of the current study is to develop a scaling for the hydrodynamic velocity fluctuations and their relaxation times, which are two of the key parameters for diffusion in sedimentation. To establish a scaling relationship that accounts for the effects of system size, volume fraction, and thermal fluctuations on the hydrodynamic velocity fluctuations, we calculate the temporal autocorrelation functions of the velocity fluctuations as follows:

$$C_x(t) = \langle V_{ix}(t) V_{ix}(0) \rangle \tag{7}$$

and

$$C_z(t) = \langle \delta V_{iz}(t) \delta V_{iz}(0) \rangle, \tag{8}$$

in which $\delta V_{iz} = V_{iz} - V_{\text{sed}}$, V_{iz} and V_{ix} are the temporal velocities of the ith particle in the z and x direction, respectively, and $V_{\text{sed}} = \langle V_{iz} \rangle$ is the mean settling velocity of the particles.

Figure 2 shows the time decay of the correlation functions for the z and x components of the velocity fluctuations at $\phi = 0.04$ and $L/a = 32$. The main plots in Fig. 2 use the initial fluctuations $C_z(0)$ and $C_x(0)$ as normalization constants to visualize the relaxation of the velocity fluctuations, whereas the figure insets use the square of the Stokes velocity to normalize the correlations, highlighting the effects of the nonequilibrium hydrodynamic fluctuations. Time is normalized by the Stokes time t_s such that $t_s = a/V_s^{\phi=0}$.

The main plots in Figs. 2(a) and 2(b) indicate that the large difference in relaxation times for the vertical and horizontal correlations, whereas the experiments [1] show a small difference in these time scales. The theory proposed by Koch [33] suggests that this difference between the relaxation times originates from the vertical periodic boundary conditions because less time is required for a particle to sample all vertical positions than is required to sample the horizontal positions. This difference in time scales can be reduced by increasing the aspect ratio of the periodic box or by increasing the volume fraction of the particles. The simulations performed by Ladd [10] and Padding [18] observed the same phenomena using vertical periodic boundary conditions.

At low Pe, the strong effects of the thermal fluctuations cause a rapid decay in the correlations, whereas at higher Pe, an exponential decay is evident as shown in Fig. 2. In an experimental study, Nicolai *et al.* [1] observed an exponential relaxation of the temporal correlations of velocity fluctuations of the form $C_\beta(t) = (\Delta V_{\text{H}}^\beta)^2 \exp(-t/\tau_{\text{H}}^\beta)$ in which $\Delta V_{\text{H}}^\beta$ ($\beta \in x,z$) and τ_{H}^β denote the amplitude and relaxation time of the hydrodynamic velocity fluctuations, respectively. The present DNS results support the following forms for the autocorrelations of the velocity fluctuations as the simulations are performed at finite Pe:

$$C_x(t) = C_0(t) + \left(\Delta V_{\text{H}}^x\right)^2 \exp\left(-t/\tau_{\text{H}}^x\right), \tag{9}$$

$$C_z(t) = C_0(t) + \left(\Delta V_{\text{H}}^z\right)^2 \exp\left(-t/\tau_{\text{H}}^z\right), \tag{10}$$

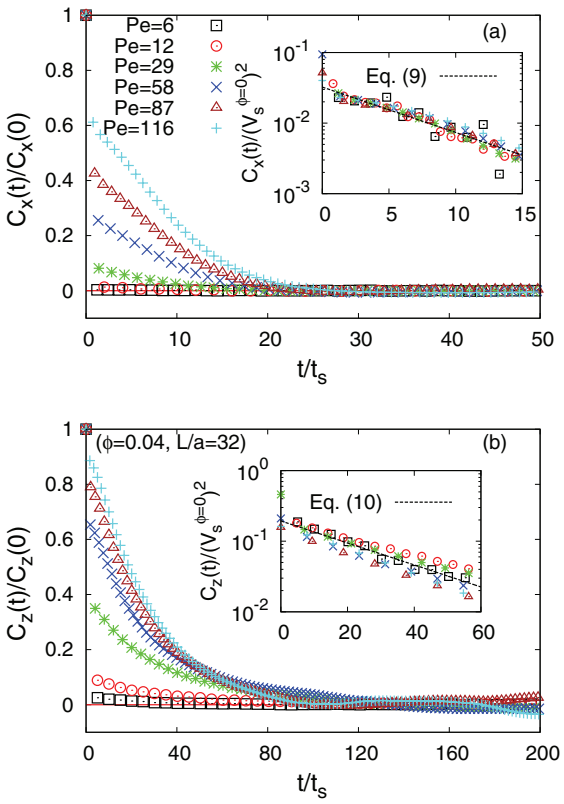

FIG. 2. (Color online) Temporal autocorrelation functions of the vertical $[C_z(t)]$ and horizontal $[C_x(t)]$ velocity fluctuations. The main plots show the correlation functions normalized by the initial fluctuations, whereas the temporal correlation functions shown in the insets are normalized by the square of the Stokes velocity on a semilog scale. The insets also indicate that at large values of Pe, these correlation functions relax exponentially according to $C_\beta(t) = (\Delta V_{\text{H}}^\beta)^2 \exp(-t/\tau_{\text{H}}^\beta)$ as shown by the dotted lines in which $\Delta V_{\text{H}}^\beta$ ($\beta \in x,z$) and τ_{H}^β denote the amplitude and the relaxation time of the hydrodynamic velocity fluctuations, respectively. Time is normalized by the Stokes time as $t_s = a/V_s^{\phi=0}$.

in which $C_0(t)$ represents the velocity autocorrelation function in the presence of thermal fluctuations but without gravity, which becomes negligible at higher Pe. These equations represent the summation of the pure thermal and hydrodynamic forces; the former is dominant at low Pe, and the latter plays a key role at high Pe. In addition to these two Pe regimes, a transition regime is also expected to exist in which neither of these two forces is dominant. Hence, the scaling relations for the diffusion coefficients based on Eqs. (9) and (10) should deviate from simulation results in this transition regime, which will be tested later.

At finite Pe, the velocity fluctuations consist of a thermal and a hydrodynamic component. The dominant role of the hydrodynamic fluctuations at higher Pe causes the correlation functions to fall on the same curve when scaled with the square of the Stokes velocity as suggested by Nicolai (see Fig. 2 insets). Our data demonstrate good agreement with the fitted curves.

We obtained the values of $\Delta V_{\text{H}}^\beta$ and τ_{H}^β at different volume fractions and system sizes from the exponential

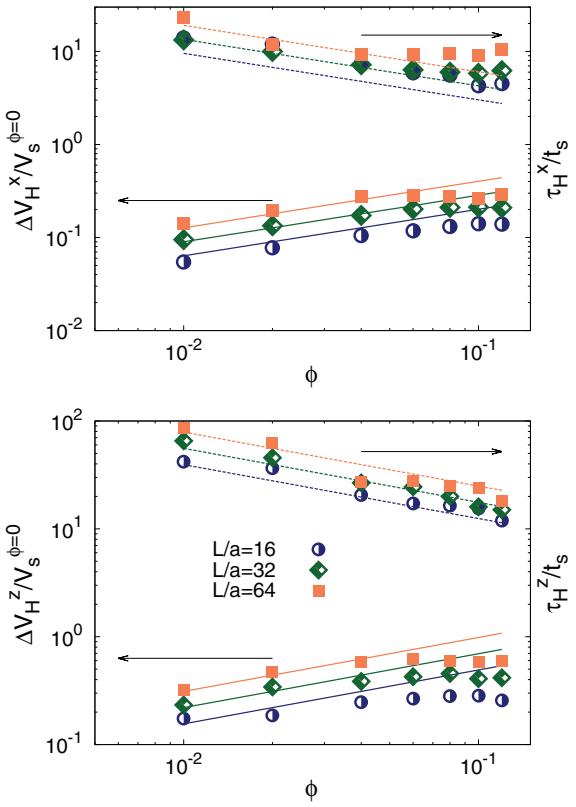

FIG. 3. (Color online) Scaling of the hydrodynamic velocity fluctuations (left scale) and their relaxation times (right scale) as a function of volume fraction, using three different system sizes: $L/a = 16, 32,$ and 64. The solid lines indicate a scaling to $\Delta V_{\mathrm{H}}^{\beta}/V_{\mathrm{s}}^{\phi=0}$ of the form $\sqrt{A_1^{\beta} L\phi/a}$, whereas the dashed lines indicate a scaling to $\tau_{\mathrm{H}}^{\beta}/t_{\mathrm{s}}$ of the form $A_2^{\beta}\sqrt{L/(\phi a)}$. The simulation results are represented by points. The symbols and lines are color coded with respect to the system size.

fits. These values are plotted in Fig. 3 for three different system sizes. Hinch [31] proposed scaling relationships for the hydrodynamic velocity fluctuations ($\Delta V_{\mathrm{H}}^{\beta}$) and their relaxation times ($\tau_{\mathrm{H}}^{\beta}$). Cunha *et al.* [19] explained this scaling by hypothetically dividing the simulation box into two equal parts. The imbalance in the particle weight caused by variations in the particle number in both parts is balanced by the Stokes drag. They predicted the scaling relations as $\Delta V_{\mathrm{H}}^{\beta}/V_{\mathrm{s}}^{\phi=0} = \sqrt{A_1^{\beta} L\phi/a}$ and $\tau_{\mathrm{H}}^{\beta}/t_{\mathrm{s}} = A_2^{\beta}\sqrt{L/(\phi a)}$ in which A_1^{β} and A_2^{β} are constants that depend on the system parameters (e.g., the container shape, swirl size, particle shape, and polydispersity). This simple scaling is expected to work well for low volume fractions.

The prefactors A_1^{β} and A_2^{β} are obtained by fitting the scaling relationships to the simulation data, as shown in Fig. 3, which demonstrates the scaling of the hydrodynamic velocity fluctuations and their relaxation times as a function of the volume fraction for three different system sizes both in the x and z direction. Our simulation results are in good agreement with the scaling relations in the low volume fraction regime, but deviations are evident in the moderate volume fraction for all system sizes. Figure 3 also depicts that, for a given system size, $\Delta V_{\mathrm{H}}^{\beta}$ and τ_{H}^{x} reach a saturation value at moderate volume fractions. The simulations of Padding *et al.* [18], Cunha *et al.* [19], and the rationalized results [9] (considering the side wall effects) of Segre *et al.* [4] also demonstrated similar scaling at low volume fractions. Cunha showed the transition from $\phi^{1/2}$, but unfortunately the scaling was unclear at high volume fraction. In contrast, Brenner [9] theoretically proposed the transition from $\phi^{1/2}$ to $\phi^{1/3}$, which is not confirmed by any other simulation or experimental study. In contrast to τ_{H}^{x}, τ_{H}^{z} follows the $\phi^{-1/2}$ scaling for the full range of volume fraction. Kuusela *et al.* [24] and Padding *et al.* [18] found a similar scaling relation in their studies. This different decay pattern in the vertical direction is attributed to enhanced memory effects in the direction of flow. In contrast, experiments of Nicolai *et al.* [1] did not find any clear decay pattern. It is well known [9] that experiments are affected by many nonideal conditions, such as secondary flow, instability, side wall effects, and polydispersity. These nonideal conditions, especially polydispersity and side walls, greatly affect the relaxation time [9,14].

The velocity fluctuations and their relaxation times in both directions scale as $(L/a)^{1/2}$ for the full range of volume fractions studied, indicating that our simulations are in a spatially correlated regime. The relevant scaling effects induced by the size dependence of this finite system are discussed in detail in Sec. IV C. The summary of the scaling is presented in Table I.

These findings at moderate volume fraction lead us to split the scaling relationships into two: one for low volume fractions ($\phi \leqslant 0.04$), similar to that observed in other studies [9,18,19], and a second for moderate volume fractions ($0.06 \leqslant \phi \leqslant 0.12$) as shown in Eqs. (11)–(13):

$$\Delta V_{\mathrm{H}}^{\beta}/V_{\mathrm{s}}^{\phi=0} = \begin{cases} \sqrt{A_1^{\beta} L\phi/a}, & (\phi \leqslant 0.04) \\ \sqrt{A_1^{\beta} L\phi_{\mathrm{sat}}^{V_\beta}/a}, & (0.06 \leqslant \phi \leqslant 0.12) \end{cases} \tag{11}$$

$$\tau_{\mathrm{H}}^{x}/t_{\mathrm{s}} = \begin{cases} A_2^{x}\sqrt{L/(\phi a)}, & (\phi \leqslant 0.04) \\ A_2^{x}\sqrt{L/\left(\phi_{\mathrm{sat}}^{\tau_x} a\right)} & (0.06 \leqslant \phi \leqslant 0.12) \end{cases}, \tag{12}$$

and

$$\tau_{\mathrm{H}}^{z}/t_{\mathrm{s}} = \left\{ A_2^{z}\sqrt{L/(\phi a)}, \quad (\phi \leqslant 0.12), \right. \tag{13}$$

in which $\phi_{\mathrm{sat}}^{V_\beta}$ provides the saturation value of the hydrodynamic velocity fluctuations with respect to the volume fraction in both the x and z directions at moderate volume fractions.

TABLE I. Summary of the scaling obtained for the hydrodynamic velocity fluctuations ($\Delta V_H^{\beta}/V_{\mathrm{s}}^{\phi=0}$) and their relaxation times ($\tau_H^{\beta}/t_{\mathrm{s}}$) in both the vertical and horizontal directions. In addition to the above scaling, both $\Delta V_H^{\beta}/V_{\mathrm{s}}^{\phi=0}$ and $\tau_H^{\beta}/t_{\mathrm{s}}$ are scaled as $(L/a)^{1/2}$ with system size in the low to moderate volume fraction regimes.

	Scaling of $\Delta V_H^{\beta}/V_{\mathrm{s}}^{\phi=0}$ and $\tau_H^{\beta}/t_{\mathrm{s}}$	
	Low ϕ ($\phi \leqslant 0.04$)	Moderate ϕ ($0.06 \leqslant \phi \leqslant 0.12$)
$\Delta V_H^{x}/V_{\mathrm{s}}^{\phi=0}$	$\sim\phi^{1/2}$	$\sim\phi^{0}$
$\Delta V_H^{z}/V_{\mathrm{s}}^{\phi=0}$	$\sim\phi^{1/2}$	$\sim\phi^{0}$
$\tau_H^{x}/t_{\mathrm{s}}$	$\sim\phi^{-1/2}$	$\sim\phi^{0}$
$\tau_H^{z}/t_{\mathrm{s}}$	$\sim\phi^{-1/2}$	$\sim\phi^{-1/2}$

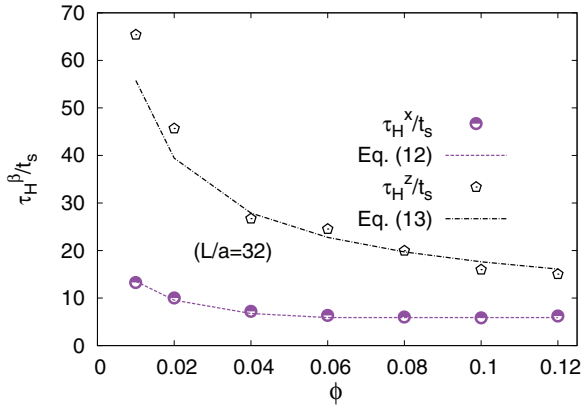

FIG. 4. (Color online) Hydrodynamic velocity fluctuation relaxation times for both the vertical and horizontal directions as a function of volume fraction. The dashed line indicates the scaling of τ_H^x/t_s and the dot-dashed line indicates the scaling of τ_H^z/t_s. The simulation data are represented by points. This plot shows that the difference in the vertical and horizontal relaxation times decreases with increasing volume fraction at moderate volume fraction regimes. Our data show good agreement with the scaling Eqs. (12) and (13).

Furthermore, $\phi_{\rm sat}^{\tau_x}$ is the saturation value of the relaxation time in the x direction only, as vertical relaxation times obey the corresponding scaling for the full range of volume fractions as evident in Eqs. (12) and (13). Similar phenomena have been observed by Ladd [10] in a simulation study in which no change was found in the horizontal relaxation time at $\phi = 0.05$ and $\phi = 0.25$, but the vertical relaxation time decreased at these volume fractions. In the same study, Ladd also reported a saturation of the vertical relaxation times at high volume fractions ($\phi \geqslant 0.45$). In an experimental study, Bernard *et al.* [53] explored the dependency of the relaxation time on the volume fraction and system size and determined that the relaxation time scaled as $(L/a)^{0.65\pm0.1}$, in agreement with the $(L/a)^{0.5}$ scaling observed in this study. Unlike the present study, Bernard found no systematic dependency of the relaxation time on the volume fraction.

The different scaling of the vertical and horizontal relaxation times at moderate volume fractions leads to a decrease in the difference between the vertical and horizontal relaxation times with increasing volume fraction as shown in Fig. 4. This finding is important because it aids in characterizing the anisotropic nature of diffusion. Further discussion on the effect of this decrease is presented in Sec. IV B. Our data show good consistency with the scaling Eqs. (11)–(13).

The prefactors A_1^β and A_2^β are determined from the fits to be $A_1^z \approx 0.151$, $A_2^z \approx 0.9857$, $A_1^x \approx 0.0253$, and $A_2^x \approx 0.239$ at low volume fractions. For moderate volume fractions, we extracted the values of $\phi_{\rm sat}^{V_\beta}$ and $\phi_{\rm sat}^{\tau_x}$ by fitting the scaling relationships and obtained $\phi_{\rm sat}^{V_z} = 0.037$, $\phi_{\rm sat}^{V_x} = 0.05135$, and $\phi_{\rm sat}^{\tau_x} = 0.0526$. The values of these fitting coefficients are also summarized in Table II. The differences in the vertical and horizontal prefactors indicate the anisotropic behavior of the velocity fluctuations, with vertical fluctuations larger than the horizontal ones. This anisotropy in the velocity fluctuations varies from 2.5 to 4 in the simulations [10,12,19,21]. The experiments [1,4] have provided a value of ≈2.5. Notably, the ratio of the vertical to horizontal hydrodynamic velocity fluctuations in this study is $\Delta V_{\rm H}{}^z/\Delta V_{\rm H}{}^x \approx 2.44$ at low volume fractions, and 2.07 at moderate volume fractions, which are in good agreement with the experimental [1,4] and simulation [21] results. This anisotropic behavior in the velocity fluctuations is believed to be due to the asymmetry of the system induced by gravity.

TABLE II. A quantitative comparison of the fitting coefficients obtained by fitting Eqs. (11)–(13) onto the simulation data. The difference between the x- and z-direction coefficients indicates the anisotropic nature of the phenomena.

Scaling coefficients	Values
A_1^x	0.0253
A_2^x	0.239
A_1^z	0.151
A_2^z	0.9857
$\phi_{\rm sat}^{V_x}$	0.0514
$\phi_{\rm sat}^{V_z}$	0.037
$\phi_{\rm sat}^{\tau_x}$	0.0526

B. Scaling and anisotropic behavior of diffusion

Diffusion occurs due to the fluctuating motion of particles. Individual particles lose the memory of their velocity after experiencing hydrodynamic interactions with surrounding particles and thereafter follow a random-walk diffusion process. To find the scaling of a long-time steady-state self-diffusion coefficient, we consider the total diffusion coefficient D as the sum of the thermal contribution D_0 and the hydrodynamic contribution $D_{\rm H}$, where the latter is estimated as

$$D_{\rm H}^\beta \approx \left(\Delta V_{\rm H}^\beta\right)^2 \tau_{\rm H}^\beta. \tag{14}$$

Based on the aforementioned scaling relationships for $\Delta V_{\rm H}^\beta$ and $\tau_{\rm H}^\beta$, for both low and moderate volume fraction regimes, we can also find the scaling for the diffusion coefficients in the z and x directions:

$$D_z/D_0 = \begin{cases} 1 + A_1^z A_2^z {\rm Pe}\,(L/a)^{3/2}\,\phi^{1/2} = 1 + 0.149{\rm Pe}\,(L/a)^{3/2}\,\phi^{1/2}, & (\phi \leqslant 0.04) \\ 1 + A_1^z A_2^z \phi_{\rm sat}^{V_z} {\rm Pe}\,(L/a)^{3/2}\,\phi^{-1/2} = 1 + 0.0056{\rm Pe}\,(L/a)^{3/2}\,\phi^{-1/2}, & (0.06 \leqslant \phi \leqslant 0.12) \end{cases}, \tag{15}$$

$$D_x/D_0 = \begin{cases} 1 + A_1^x A_2^x {\rm Pe}\,(L/a)^{3/2}\,\phi^{1/2} = 1 + 0.006{\rm Pe}\,(L/a)^{3/2}\,\phi^{1/2}, & (\phi \leqslant 0.04) \\ 1 + A_1^x A_2^x \phi_{\rm sat}^{V_x} \left(\phi_{\rm sat}^{\tau_x}\right)^{-1/2} {\rm Pe}\,(L/a)^{3/2} = 1 + 0.0013{\rm Pe}\,(L/a)^{3/2}, & (0.06 \leqslant \phi \leqslant 0.12) \end{cases}. \tag{16}$$

TABLE III. Summary of the scaling obtained for the self-diffusion coefficients (D_β/D_0) in both the vertical and horizontal directions. Additionally, diffusion coefficients in both directions scale as $(L/a)^{3/2}$ with system size and linearly with Pe.

	Scaling of D_β/D_0	
	Low ϕ ($\phi \leqslant 0.04$)	Moderate ϕ ($0.06 \leqslant \phi \leqslant 0.12$)
D_x/D_0	$\sim\phi^{1/2}$	$\sim\phi^{0}$
D_z/D_0	$\sim\phi^{1/2}$	$\sim\phi^{-1/2}$

These scaling relations indicate that the vertical and horizontal diffusion coefficients increase linearly with Pe, but with a smaller prefactor in the horizontal direction. In addition, they scale as $(L/a)^{3/2}$ with the system size for the full range of volume fractions that we have considered. Furthermore, both the vertical and horizontal diffusion coefficients scale with $\phi^{1/2}$ at low volume fraction, but at moderate volume fraction the diffusion coefficient in the vertical direction scales as $\phi^{-1/2}$, and the horizontal diffusion coefficient becomes independent of volume fraction. This additional dependency on $\phi^{-1/2}$ in the vertical direction causes a decrease in the diffusion anisotropy with increasing volume fraction. The scaling relations for the diffusion coefficients are summarized in Table III.

The long-time steady-state self-diffusion coefficient [$D_\beta = \lim_{t\to\infty} D_\beta(t)$] is obtained from the linear growth of the mean-square displacement (MSD) in the horizontal and vertical directions as follows:

$$D_x(t) = \frac{1}{2t}\langle (R_{ix}(t) - R_{ix}(0))^2 \rangle, \tag{17}$$

$$D_z(t) = \frac{1}{2t}\langle (R_{iz}(t) - R_{iz}(0) - V_{\text{sed}}t)^2 \rangle. \tag{18}$$

The equilibrium self-diffusion coefficient can be obtained using the Einstein relationship:

$$D_0 = \lim_{t\to\infty} \frac{1}{6t}\langle (\boldsymbol{R}_i(t) - \boldsymbol{R}_i(0))^2 \rangle. \tag{19}$$

Figure 5 shows a comparison of the long-time steady-state self-diffusion coefficients with the scaling relations. Figures 5(a) and 5(b) show the diffusion coefficient as a function of Pe in the horizontal direction for low and moderate volume fractions, respectively. Figures 5(c) and 5(d) show the diffusion coefficient in the vertical direction as a function of Pe for low and moderate volume fractions, respectively. Figures 5(a) and 5(c) indicate that the diffusion coefficient increases with increasing volume fraction both in the horizontal and vertical directions at low volume fractions. In contrast with the low volume fraction regime, the vertical diffusion coefficient decreases with increasing volume fraction at moderate volume fractions as shown in Fig. 5(d). Figure 5(b) demonstrates no change in the horizontal diffusion coefficient. This decrease in the vertical diffusion coefficient is attributed to the $\phi^{-1/2}$ scaling of τ_{H}^z. However, due to the saturation of τ_{H}^x and ΔV_{H}^x at moderate volume fraction, no change is observed in the horizontal diffusion coefficient.

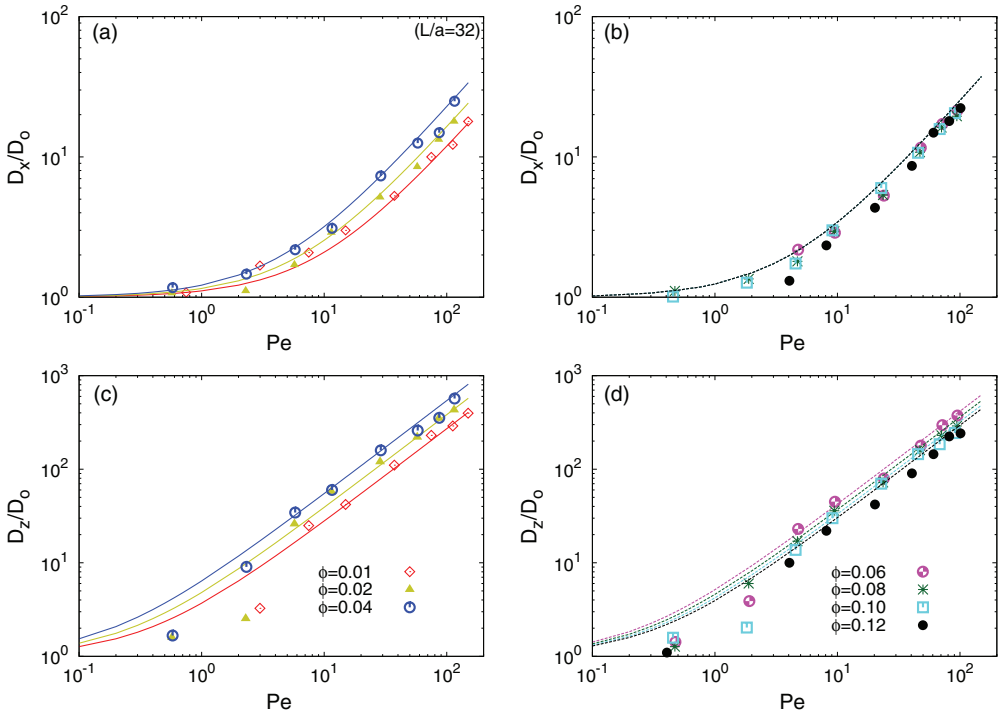

FIG. 5. (Color online) A comparison of the long-time steady-state self-diffusion coefficients in both the vertical and horizontal directions with those predicted by the scaling Eqs. (15) and (16) as a function of Pe. The self-diffusion coefficients are normalized by the equilibrium diffusion coefficient D_0. (a) and (b) show the scaling of D_x/D_0 for low and moderate volume fractions, respectively, whereas (c) and (d) show the scaling of D_z/D_0 for low and moderate volume fractions, respectively. The simulation results are represented by points. The lines indicate the scaling relations. The symbols and lines are color coded with respect to the volume fraction.

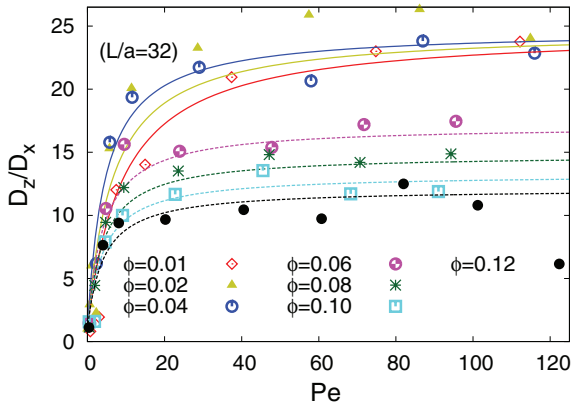

FIG. 6. (Color online) The anisotropy of the vertical (D_z) and horizontal (D_x) self-diffusion coefficients as a function of Pe for different volume fractions. The solid lines indicate the scaling of D_z/D_x at low volume fractions, whereas the dashed lines indicate the scaling at moderate volume fractions. The scaling lines are obtained by dividing Eq. (15) with Eq. (16) for the respective volume fraction regime. Lines and points of the same color indicate the results for the same volume fraction.

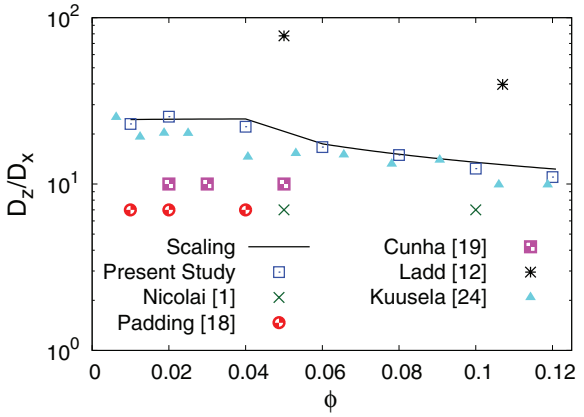

FIG. 7. (Color online) Comparison of the diffusion anisotropy with the scaling and previously published experimental and simulated data. Nicolai [1] obtained the low anisotropy value in an experimental study in a spatially screened regime, whereas Cunha [19] and Padding [18] achieved these results from the DNS and SRD using a periodic box with an aspect ratio of 3. A relatively large value of anisotropy is achieved due to cubic periodic box and spatially unscreened regime. Our data show good agreement with the simulation study of Kuusela *et al.* [24] and the scaling.

Our simulation results indicate that the diffusion coefficients increase linearly with increasing Pe, both parallel and perpendicular to gravity. A deviation from the scaling relations is evident at low Pe. Because scaling relations are derived by adding pure thermal and hydrodynamic forces, these relations are expected to show good agreement with the simulation results when either thermal or hydrodynamic fluctuations dominate the phenomena. Hence, this deviation indicates the transition regime in which neither force is dominant. Our simulations show good agreement with Eqs. (15) and (16) at high Pe, demonstrating the dominance of the hydrodynamic interactions.

The majority of studies [1,4,10,19,23,53] on particle diffusion in sedimentation have focused on the non-Brownian regime. Particle diffusion and its anisotropic nature at finite Pe values have not yet been explored. We have attempted to investigate this anisotropic behavior and found that, for a given volume fraction, the anisotropy increases with increasing Pe, becoming saturated at higher Pe as shown in Fig. 6. This observation suggests that the effect of thermal fluctuations is significant at low Pe before the HIs begin to dominate the sedimentation phenomenon. We can predict the anisotropic behavior of the diffusion at finite Pe with scaling relationships. Our data show good agreement with the predicted diffusion anisotropy as indicated in Fig. 6. Furthermore, the scaling relationships suggest that the saturated or steady-state value of the anisotropy remains unchanged at low volume fractions and decreases with increasing volume fraction at moderate volume fractions as shown in Fig. 6. This decrease in anisotropy is attributed to the decrease in the difference between the vertical and horizontal relaxation times. This difference is decreased by the $\phi^{-1/2}$ scaling of the vertical relaxation time at moderate volume fractions. The horizontal relaxation time is independent of volume fraction in this regime as shown in Table I.

Our simulation results are also compared with the previous experimental and simulation results in Fig. 7, which shows the diffusion anisotropy as a function of the volume fraction. Nicolai [1] obtained these results in a spatially screened regime, whereas Cunha [19] and Padding [18] performed DNS and SRD simulations in an elongated simulation box with an aspect ratio of 3. We have obtained a relatively high value of the anisotropy at a low volume fraction. This higher value originates from the difference in vertical and horizontal relaxation times. Because diffusivity is the product of ΔV_H^2 and τ_H, a larger difference in relaxation time leads to a higher diffusion anisotropy. The diffusion anisotropy can be reduced by increasing the aspect ratio of the simulation box [33]. An increase in the aspect ratio reduces this difference and thus the diffusion anisotropy, as exhibited by Cunha [19] and Padding [18]. In addition, increasing the aspect ratio reduces the prefactors of Eqs. (15) and (16), especially in the vertical direction [33], which in turn reduces the diffusion anisotropy. Hence, diffusion anisotropy is not only dependent on volume fraction, it also depends on the aspect ratio of the cell. We obtained an anisotropy of ≈24, whereas Cunha and Padding found this anisotropy to be ≈10 and 7, respectively, at low volume fractions. In another simulations study [24], Kuusela *et al.* obtained large diffusion coefficients in both directions using a 2D periodic square simulation box, but the ratio of diffusion coefficients shows good agreement with our results. In contrast with the present study, Nicolai [1] obtained an anisotropy of ≈7 and found no decrease in the anisotropy at moderate volume fractions, primarily because they obtained their results in a large container, which is many times greater than the correlation length. In simulations, the use of such a large system is impossible due to the large computational cost. Another possible explanation for the discrepancy between the simulations and the experimental results is the presence of a side wall in the experiments, which creates microstructural inhomogeneities over time [9,54]. In addition, the presence of polydispersity, even to a small extent, can temper the diffusion. Ladd [12] obtained a high anisotropy ≈77 at $\phi = 0.05$. This

large value is attributed to the small system size and the use of full periodic boundary conditions. Similar to the present study, Ladd [12] demonstrated that diffusion anisotropy decreases with increasing volume fraction. The anisotropy of diffusion, which was ≈77 at $\phi \approx 0.05$, decreased to ≈39 at $\phi \approx 0.107$. We have many experimental and simulation studies to compare with at low volume fractions, but unfortunately, we could not find a study which had addressed the scaling of diffusion anisotropy with respect to volume fraction at moderate or transition regime.

C. Finite size effects

Theoretical arguments [7] and simulations [12] have long exhibited the strong dependency of velocity fluctuations on the system size for a random suspension of particles. In contrast, experiments [1–3,5] show no such divergence. This disagreement was solved by Segre *et al.* [4] who suggested that the velocity fluctuations increase with the system size only when the system size is smaller than the correlation length, and above this correlation length, the simulations and experiments should be in good agreement. Experimentation has the freedom to use large system sizes, whereas in simulations, large systems require enormous resources. Thus, most simulation studies [10,18,19,21] are affected by the artifacts induced by the finite system size. To observe the system size dependency in our results, we defined the spatial correlation function of the velocity fluctuations, which defines the flow pattern of the particles as follows:

$$C_z(\boldsymbol{r}) = \frac{2L^3}{N^2}\left\langle \sum_{i<j} \delta V_{iz}\delta V_{jz}\delta(\boldsymbol{r}-\boldsymbol{r}_{ij})\right\rangle. \qquad (20)$$

We define $C_z(z)$ and $C_z(x)$, with respect to the distance vector $\boldsymbol{r}$, in either the vertical $\boldsymbol{r} = z\boldsymbol{\delta}_z$ or horizontal $\boldsymbol{r} = x\boldsymbol{\delta}_x$ direction.

We plotted the spatial correlation function of the z component of the velocity as a function of the distance perpendicular to gravity in Fig. 8 using three different cubic boxes L/a =16, 32, and 64, at $\phi = 0.10$. Figure 8 shows that the velocity

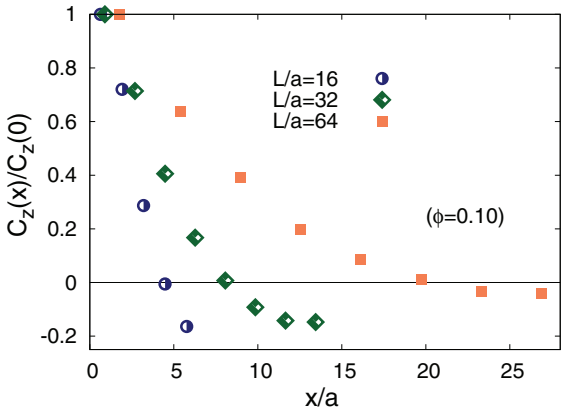

FIG. 8. (Color online) Spatial correlation function of the z component of velocity as a function of the distance perpendicular to gravity, demonstrating the effects of system size on velocity fluctuations. All simulations were performed at a volume fraction of $\phi \approx 0.10$ and Pe ≈ 80.

fluctuations become long ranged with an increase in the system size, which is in agreement with the tendencies observed in similar simulation studies [18,24]. Our simulation results support the experimental findings of Segre [4] when the system size is smaller than the correlation length. Therefore, the particle motion should be affected by the finite system in our simulations. Figure 8 shows that a large system size is needed to reproduce the saturation of the velocity fluctuations, but this requires enormous computational time and resources. Therefore, most of the computational studies [10,11,14,18,19] are similarly limited. Systematic experimental [2,4] and simulation [11,13] studies, however, have revealed that the effects of finite system size on velocity fluctuations can be effectively explained using the concept of finite-size scaling [18]. We believe that there is value in performing critical tests on the scaling concept. In addition, the experiments [2,4] and simulations [11,13] addressing the effects of finite system size on velocity fluctuations have also established that finite system size may lead to smaller velocity fluctuations [18].

V. CONCLUSION

We studied steady-state sedimentation at a finite Peclet number using the direct numerical simulations with the smooth-profile method in a spatially unscreened regime. The present study focused on the scaling of hydrodynamic velocity fluctuations and self-diffusivities with respect to volume fraction and system size. The study also examined the relative effects of thermal and hydrodynamic fluctuations. We observed a clear transition from a Brownian-motion-dominant regime to a hydrodynamic-fluctuations-dominant regime. Moreover, the hydrodynamic velocity fluctuations increased with increasing volume fraction at low volume fraction ($\phi \leqslant 0.04$) in accordance with theoretical predictions [7,9] and previous studies [18,19], whereas at moderate volume fraction ($0.06 \leqslant \phi \leqslant 0.12$), their behavior was independent of ϕ, similar to Nicolai *et al.* [1] and Climent *et al.* [25]. We concluded that the amplitudes of the velocity fluctuation correlations scale with the square of the Stokes velocity at large Pe, with vertical hydrodynamic velocity fluctuations that are ≈2.5 times larger than the horizontal hydrodynamic velocity fluctuations at low volume fractions, in good agreement with other studies [1,18,19,25]. At moderate volume fractions, this value drops to ≈2. In addition, we tested the scaling relations for the hydrodynamic velocity fluctuations suggested by Hinch [31] for different system sizes and volume fractions. We found that this scaling worked well for low volume fractions and deviated at moderate volume fraction regimes.

Consistent with the theoretical predictions [7,9], we found that both the vertical and horizontal velocity fluctuations scale as $(\phi L/a)^{1/2}$ at low volume fractions, saturating with respect to ϕ at moderate volume fractions. Similarly, the horizontal velocity fluctuation relaxation time scales as $(L/a\phi)^{1/2}$ at low volume fractions, saturating with respect to ϕ at moderate volume fractions. This result is in contrast with that of the vertical relaxation time, which scales as $(L/a\phi)^{1/2}$ for both regimes. Padding *et al.* [18] and Kuusela *et al.* [24] observed a similar decay behavior for vertical relaxation time. Furthermore, we found that the difference in the vertical and horizontal hydrodynamic velocity fluctuation relaxation times

decreased with increasing volume fraction at moderate volume fractions.

Based on the scaling of the hydrodynamic velocity fluctuations and their relaxation times, we inferred the scaling relations of the long-time steady-state self-diffusion coefficient for both low and moderate volume fraction regimes. Theoretical arguments [7,9,19] suggest that both the vertical and horizontal self-diffusion coefficients scale as $(L/a)^{3/2}\phi^{1/2}$ at low volume fractions. Our results have shown the similar behavior. In contrast to the low volume fraction regimes, the vertical self-diffusion coefficient scales as $(L/a)^{3/2}\phi^{-1/2}$ at moderate volume fractions, due to a decrease in the vertical relaxation time with volume fraction, whereas the horizontal diffusion coefficient is saturated with respect to ϕ in this regime. Our simulation results found good consistency with the scaling relations. These relations in hydrodynamic velocity fluctuations, their relaxation times, and the self-diffusion coefficients are summarized in Tables I and III. The scaling of the diffusion coefficients allows us to predict the anisotropy of the vertical and horizontal diffusion. We found that the diffusion anisotropy increases with increasing Pe, saturating at high Pe, in accordance with Ref. [18]. This saturated value remains unchanged at low volume fractions and decreases with increasing volume fraction at moderate volume fractions. The decrease in the anisotropy with volume fraction is induced by the decrease in the difference in magnitudes of the vertical and horizontal hydrodynamic relaxation times. We obtained a relatively high anisotropy at low volume fraction. This higher value is attributed to the use of a cubic periodic box, as an increase in aspect ratio reduces the diffusion anisotropy [18,19,33].

The present simulations were performed maintaining $\mathrm{Re} < 0.2$, so that the inertial effects are negligible. Extensive simulations are underway to study the effects of inertial forces at moderate Re values. Additionally, we are attempting to simulate even higher volume fractions for non-Brownian particles to study the behavior of velocity fluctuations and particle diffusion.

ACKNOWLEDGMENTS

This work was supported by KAKENHI 23244087 and the Global COE Program, "International Center for Integrated Research and Advanced Education in Materials Science" from the Ministry of Education, Culture, Sports, Science and Technology of Japan. The author would like to extend his gratitude to Dr. Takahiro Murashima, Dr. Hideyuki Mizuno, and Dr. John Molina for their useful discussions and suggestions.

[1] H. Nicolai, B. Herzhaft, E. J. Hinch, L. Oger, and E. Guazzelli, Phys. Fluids **7**, 12 (1995).
[2] H. Nicolai and E. Guazzelli, Phys. Fluids **7**, 3 (1995).
[3] H. Nicolai, Y. Peysson, and E. Guazzelli, Phys. Fluids **8**, 855 (1996).
[4] P. N. Segre, E. Helbolzheimer, and P. M. Chaikin, Phys. Rev. Lett. **79**, 2574 (1997).
[5] P. N. Segrè, F. Liu, P. Umbanhowar, and D. A. Weitz, Nature (London) **409**, 594 (2001).
[6] P. N. Segre, Phys. Rev. Lett. **89**, 254503 (2002).
[7] R. E. Caflish and J. H. C. Luke, Phys. Fluids **28**, 759 (1985).
[8] D. L. Koch and E. S. G. Shaqfeh, J. Fluid Mech. **224**, 275 (1991).
[9] M. P. Brenner, Phys. Fluids **11**, 754 (1999).
[10] A. J. C. Ladd, Phys. Fluids A **5**, 299 (1993).
[11] A. J. C. Ladd, Phys. Rev. Lett. **76**, 1392 (1996).
[12] A. J. C. Ladd, Phys. Fluids **9**, 491 (1997).
[13] A. J. C. Ladd, Phys. Rev. Lett. **88**, 048301 (2002).
[14] N. Q. Nguyen and A. J. C. Ladd, J. Fluid Mech. **525**, 73 (2005).
[15] A. J. C. Ladd and R. Verberg, J. Stat. Phys. **104**, 1191 (2001).
[16] J. T. Padding and A. A. Louis, Phys. Rev. Lett. **93**, 220601 (2004).
[17] J. T. Padding and A. A. Louis, Phys. Rev. E **74**, 031402 (2006).
[18] J. T. Padding and A. A. Louis, Phys. Rev. E **77**, 011402 (2008).
[19] F. R. Cunha, G. C. Abade, A. J. Sousa, and E. J. Hinch, J. Fluids Eng. **124**, 957 (2002).
[20] S. Y. Tee, P. J. Mucha, M. P. Brenner, and D. A. Weitz, Phys. Fluids **19**, 113304 (2007).
[21] M. C. Miguel and R. Pastor-Satorras, Europhys. Lett. **54**, 45 (2001).
[22] Y. Xiaolong and D. L. Koch, Phys. Fluids **20**, 043305 (2008).
[23] E. Kuusela, J. M. Lahtinen, and T. Ala-Nissila, Phys. Rev. E **69**, 066310 (2004).
[24] E. Kuusela and T. Ala-Nissila, Phys. Rev. E **63**, 061505 (2001).
[25] E. Climent and M. R. Maxey, Int. J. Multiphase Flow **29**, 579 (2003).
[26] G. K. Batchelor, J. Fluid Mech. **52**, 245 (1972).
[27] G. G. Stokes, *Mathematical and Physical Papers* (Johnson Reprint Corporation, New York, 1966).
[28] J. M. Ham and G. M. Homsy, Int. J. Multiphase Flow **14**, 533 (1988).
[29] R. H. Davis, J. Fluid Mech. **310**, 325 (1996).
[30] A. Levine, S. Ramaswamy, E. Frey, and R. Bruinsma, Phys. Rev. Lett. **81**, 5944 (1998).
[31] E. J. Hinch, in *Disorder and Mixing*, edited by E. Guyon, Y. Pomeau, and J. P. Nadal (Kluwer Academic, Dordrecht, 1988).
[32] E. Guazzelli and J. Hinch, Annu. Rev. Fluid Mech. **43**, 97 (2011).
[33] D. L. Koch, Phys. Fluids **6**, 2894 (1994).
[34] J. W. Swan, J. F. Brady, V. N. Michailidou, and G. Petekidis, Phys. Rev. Lett. **109**, 068302 (2009).
[35] P. J. Hoogerbrugge and J. M. V. A. Koelman, Europhys. Lett. **19**, 155 (1992).
[36] Y. Nakayama and R. Yamamoto, Phys. Rev. E **71**, 036707 (2005).
[37] H. Tanaka and T. Araki, Phys. Rev. Lett. **85**, 1338 (2000).
[38] A. Hamid and R. Yamamoto, J. Phys. Soc. Jpn. **82**, 024004 (2013).
[39] A. Hamid and R. Yamamoto, AIP Conf. Proc. **1518**, 444 (2013).
[40] Y. Nakayama, K. Kim, and R. Yamamoto, Eur. Phys. J. E **26**, 361 (2008).
[41] T. Iwashita, Y. Nakayama, and R. Yamamoto, J. Phys. Soc. Jpn. **77**, 074007 (2008).
[42] T. Iwashita and R. Yamamoto, Phys. Rev. E **79**, 031401 (2009).
[43] Y. Nakayama, K. Kim, and R. Yamamoto, Adv. Powder Technol. **21**, 206 (2010).

[44] KAPSEL website, http://www-tph.cheme.kyoto-u.ac.jp/kapsel/.
[45] A. A. Zick and G. M. Homsy, J. Fluid Mech. **115**, 13 (1982).
[46] X. Luo, R. Martin, M. R. Maxey, and G. E. Karniadakis, J. Comp. Phys. **228**, 1750 (2009).
[47] M. R. Maxey and B. K. Patel, Int. J. Multiphase Flow **27**, 1603 (2001).
[48] R. M. Kirby, T. C. Warburton, I. Lomtev, and G. E. Karniadakis, Appl. Numer. Math. **33**, 393 (2000).
[49] D. C. Rapaport, in *The Art of Molecular Dynamics Simulation*, 2nd ed. (Cambridge University Press, Edinburgh, 2004), pp. 90–91.
[50] G. Bossis and J. F. Brady, J. Chem. Phys. **87**, 5437 (1987).
[51] M. S. Wertheim, Phys. Rev. Lett. **10**, 321 (1963).
[52] E. Thiele, J. Chem. Phys. **39**, 474 (1963).
[53] G. Bernard-Michel, A. Monavon, D. Lhuillier, D. Abdo, and H. Simon, Phys. Fluids **14**, 2339 (2002).
[54] Y. Peysson and E. Guazzelli, Phys. Fluids **10**, 44 (1998).